JOURNAL OF GEOPHYSICAL RESEARCH, VOL. 103, NO. C12, PAGES 27,739–27,752, NOVEMBER 15, 1998

The effect of included particulates on the spectral albedo of sea ice

B. Light
Department of Atmospheric Sciences, University of Washington, Seattle

H. Eicken[1]
Alfred-Wegener-Institut für Polar und Meeresforschung, Postfach, Bremerhaven, Germany

G. A. Maykut and T. C. Grenfell
Department of Atmospheric Sciences, University of Washington, Seattle

Abstract. Sediments and other particulates are often entrained into sea ice formed over shallow shelves in the Arctic, causing significant changes in the albedo of the ice and in the amount of shortwave radiation absorbed and transmitted by the ice. A structural-optical model was used in conjunction with a four-stream radiative transfer model to examine the effects of such particulates on the optical properties of sea ice. Albedo data from well-characterized ice with moderate particulate loading were combined with model calculations to infer a spectral absorption coefficient and effective size for the particulates. Results indicate that sediment particles contained in the ice have an effective radius (R) of ~9 μm, assuming absorption coefficients similar to those of Saharan dust. With these values, model predictions are in close agreement with spectral albedo observations over a broad range of particulate loading. For particle size distributions commonly observed in sea ice, the calculations indicate that particles with $R > 30$ μm have little effect on the bulk optical properties of the ice. The albedo data also suggest that even apparently "clean" ice contains trace amounts (5–10 g m^{-3}) of particulates that reduce albedos by as much as 5–10% in the visible part of the spectrum. The calculations show that particulates in sea ice primarily affect radiative transfer at visible wavelengths, whereas apparent optical properties in the near-infrared tend to be governed by ice structure rather than by the presence of particulates. Particle-bearing layers occurring below ~20–30 cm are found to have little effect on albedo, although they can still have a substantial effect on transmission. Estimates of total particle loading cannot be obtained from reflectance data without some additional information on particle size, vertical distribution, and ice structure.

1. Introduction

Observations of the entrainment of sediments and other particulate matter into Siberian sea ice, and its subsequent transport by the Transpolar Drift Stream into the Nordic Seas, date back to *Nansen* [1906] and other explorers from the last century. Apart from anecdotal observations, the phenomenon of sediment-laden or "dirty" sea ice has been largely neglected until recently. Most of this recent work has been devoted to geological implications of this entrainment. A number of studies, for example, have demonstrated the importance of sea ice to sediment transport in the Arctic [*Darby et al.*, 1974; *Clark and Hanson*, 1990; *Pfirman et al.*, 1990; *Reimnitz et al.*, 1993; *Wollenburg*, 1993]. The entrainment of particulate matter into growing sea ice has also been studied in both field and laboratory experiments [*Osterkamp and Gosink*, 1984; *Reimnitz et al.*, 1990; *Ackermann et al.*, 1994]. In contrast with early observations on the small-scale distribution of sediments within the ice cover (e.g., the formation of cryoconite holes), assessments of the regional distribution of sediment-laden ice have only recently become feasible using data from icebreaker cruises into the Arctic Ocean. From these cruises, it is evident that dirty ice may account for up to 50% of the total ice coverage in some areas [*Larssen et al.*, 1987; *Pfirman et al.*, 1989; *Reimnitz et al.*, 1993; *Nürnberg et al.*, 1994].

The comparative wealth of geologically motivated work contrasts with an almost complete lack of studies to assess the significance of sediment inclusions on the mass and energy balance of the ice cover. While the most obvious effect of particle entrainment is the lowering of ice albedo, little has been done to quantify this effect. *Ledley and Thompson* [1986] calculated the effect of soot deposition on sea ice following a nuclear disaster, finding that the ice-free season was extended by 2–3.5 months. This study employed parameterizations of the optical properties of snow as a function of soot content based on results from *Warren and Wiscombe* [1985]. The impact of lowered albedo due to sediment entrainment has been estimated using a large-scale sea ice model that contained a relatively simple albedo parameterization developed by *Ledley and Pfirman* [1997]. With regard to actual field measurements, data on the total albedo of dirty ice have been obtained by *Ivanov and Alexandrov* [1994] and incorporated into estimates of areally averaged sea ice albedos [*Eicken et al.*, 1996]. Unpublished

[1]Now at Geophysical Institute, University of Alaska Fairbanks.

Paper number 98JC02587.
0148-0227/98/98JC-02587$09.00

spectral albedo measurements have also been made over sediment-laden ice in the Alaskan and Eurasian Arctic by Reimnitz and coworkers.

For particulate-laden glacial ice or snow the database is somewhat larger. *Higuchi and Nagoshi* [1977] and *Woo and Dubreuil* [1985] derived empirical relationships for the total albedo of snow as a function of mineral dust content, while the effects of different ash layer thicknesses on the ablation of a snowpack have been studied by *Driedger* [1981]. The effect of small concentrations of soot on snow albedo has been calculated by *Chylek et al.* [1983], *Warren* [1984], and *Warren and Wiscombe* [1985]. While *Gribbon* [1979] developed a simple model describing the development of cryoconite holes on glaciers based on absorption of shortwave radiation by mineral dust within the holes, *Podgorny and Grenfell* [1996] modeled the absorption of solar energy in cryoconite holes on sea ice. Finally, *Clark and Lucey* [1984] have determined the spectral reflectances of ice containing different concentrations of monomineralic inclusions.

Given the widespread occurrence of sediments and other particles within Arctic sea ice, their geological importance, and the almost complete lack of detailed information about how particulates affect absorption and scattering in the ice, this study aims to quantify how such inclusions alter the optical properties of sea ice. A four-stream, discrete-ordinates radiative transfer model is used for this purpose. Particular attention is paid to the variability of ice albedo and absorption as a function of particulate concentration, distribution, and type. A small set of field data including spectral albedo, microstructure, and physical properties of the ice column, collected from sediment-laden ice in the Eurasian Arctic, is used to validate the model and infer physical properties of the particulates.

Given the large temporal and spatial variability of dirty ice and its remote location, visible satellite data may be of particular use in determining the large-scale distribution and concentration of sediments near the ice surface. Such an application requires detailed knowledge about the effects of particulate inclusions on ice reflectance.

2. Particulate Material Within the Ice

While the presence of haze in the Arctic was first reported by *Mitchell* [1957], subsequent reports indicate that substantial concentrations of atmospherically transported material (e.g., dust and soot) are also deposited at the surface in the Arctic [*Barrie et al.*, 1981; *Rosen et al.*, 1981; *Heintzenberg*, 1982; *Noone and Clarke*, 1988]. Some of these measurements have identified elemental carbon (soot) as the dominant light absorber and suggest anthropogenic emissions as its primary source [*Rosen et al.*, 1981]. Typical concentrations of soot observed near Point Barrow, Alaska, were found to be 0.0012 g m^{-3} [*Rosen et al.*, 1981]. In addition, quantities of light-absorbing algal cells, bacteria, organic aggregates colonized by bacteria, dissolved material, and detrital particles are often found throughout the ice and snow pack. Interior algal communities occur in relatively small concentrations (<0.01 g chl *a* m^{-3}) and consist of cells entrained in the ice during freezing and those that subsequently grow within the ice [*Roesler and Iturriaga*, 1994]. In the region observed during this study, the majority of particulate mass within the ice appears to have been derived from sediments, as indicated by microscopic inspection and sedimentological analysis of selected samples [*Reimnitz*, 1994]. While "clean" ice with low particulate concentrations may often contain substantial amounts of biogenic material such as fragments of diatom frustules, the bulk of particle concentrations in excess of a few tens of g m^{-3} is provided by lithogenic marine sediments [*Wollenburg*, 1993; *Nürnberg et al.*, 1994].

Although the relative importance of different entrainment mechanisms is not fully understood, observations suggest that formation of anchor and frazil ice at water depths shallower than 30 m are often associated with the incorporation of suspended particulate matter into the ice [*Osterkamp and Gosink*, 1984; *Kempema et al.*, 1989; *Reimnitz et al.*, 1993]. Fine-grained sediments interact with the underwater ice and are entrained into slush accumulating at the surface. This slush subsequently congeals into turbid ice which contains uniformly distributed sedimentary particles, mostly of silt to clay size [*Barnes et al.*, 1982; *Kempema et al.*, 1989; *Pfirman et al.*, 1990; *Reimnitz et al.*, 1993; *Nürnberg et al.*, 1994]. In visibly dirty ice, particulate concentrations commonly reach values between 100 and 200 g m^{-3} throughout an upper layer a few centimeters to a few decimeters in thickness [*Osterkamp and Gosink*, 1984; *Kempema et al.*, 1989; *Reimnitz et al.*, 1993; *Eicken et al.*, 1997].

As sediment-laden ice is subjected to surface melting during subsequent summer seasons, entrained sediments are concentrated near the surface of the ice and may subsequently collect in cryoconite holes and melt puddles [*Nansen*, 1906; *Pfirman et al.*, 1990; *Wollenburg*, 1993; *Nürnberg et al.*, 1994]. On multiyear ice, particulate concentrations in the upper 0.1 m can reach values exceeding 1000 g m^{-3}, but average concentrations in the central Arctic are generally only a few hundred g m^{-3} [*Nürnberg et al.*, 1994]. Depending on the total amount of surface ablation, a layer of concentrated sediments may still be underlain by turbid ice with undisturbed particulate inclusions. The bulk of the sediment load found in Arctic sea ice consists of terrigenous material, especially clay minerals together with significant fractions (up to 30%) of biogenic material originating both from marine sediments and from within the sea ice [*Pfirman et al.*, 1990; *Wollenburg*, 1993; *Nürnberg et al.*, 1994]. However, little is known about the physical and optical properties of sediment particles entrained in sea ice.

3. Field Measurements

During an expedition with the ice-breaking vessel R/V *Polarstern* to multiyear pack ice between Svalbard and Franz-Josef-Land in August 1993, ice properties and spectral albedos were measured at eight locations (Figure 1). Optical measurements were made with a spectral radiometer (Instrumentation Specialties Company model SR, equipped with interference-filter monochromator) having a spectral resolution of 15 nm half-bandwidth at wavelengths shorter than 750 nm and 30 nm resolution at longer wavelengths. Albedo data were obtained using a cosine collector mounted on a glass fiber-optic light guide, deployed a few decimeters above the surface. A detailed description of instrument calibration, performance, and error analysis has been given by *Berger* [1987]. The maximum cumulative error was estimated to be less than ±5% in the visible and less than ±8% in the near-infrared. In all but two cases, albedo measurements were carried out under completely overcast skies or foggy conditions, where the solar disc was not visible. This was done to avoid errors caused by short-term fluctuations in downwelling irradiance. Level ice with homogeneous surface structure was chosen for the measurements, avoiding the sector downwind of the ship's exhaust plume.

After collecting optical data, a 0.5–1.0-m long ice core was drilled at the site for determining stratigraphy and sediment content. The upper 0.25 m of the core was melted and a known volume of solution drawn through a 0.4 μm preweighed paper filter to obtain particulate mass. An ice core was also drilled completely through the floe to obtain vertical profiles of ice temperature, salinity, density, and texture. For details of ice core analysis, see *Eicken et al.* [1995]. Other measurements at these sites included integrated albedos [*Ivanov and Alexandrov*, 1994] and more detailed analysis of the particulate material [*Reimnitz*, 1994].

Thickness drilling and ice core analysis indicated that all of the measurement sites were located in multiyear ice, 2.03–3.75 m thick. Surface conditions from a typical dirty ice site are shown in Figure 2. The undisturbed surface was covered by a thin (~1 cm thickness) layer of deteriorated ice with a density of <500 kg m^{-3}. Owing to solar heating of the particulates and subsequent downward migration, this layer was relatively clean and appears quite bright because of the large amount of light backscattered. The particle-laden layer beneath the surface scattering layer can be seen in the foreground of the picture and on the ice flanks above the melt pond. The bright strip of ice along the edge of the pond was most likely caused by meltwater wash-out of sediments. Since the pond was in hydraulic connection with the ocean, the pond surface marks the freeboard level (~0.21 m below the surface). Ice above freeboard level had somewhat lower densities than ice below the freeboard due to more numerous gas bubble inclusions.

A summary of spectral albedo measurements made at three different sites is shown in Figure 3. These sites span a wide range of particulate loadings. Site A (station 227, 82°12′N, 34°30′E) had ice that appeared clean to the observer, site B (station 231, 82°23′N, 40°55′E) had ice with moderate particle loading (130 g m^{-3}), while site C (same location as A) had ice with somewhat heavier particulate loading (162 g m^{-3}). All three albedos were measured under overcast skies. Values for the clean ice at site A fall within the same range as measurements reported by *Grenfell and Maykut* [1977] and *Maykut and Perovich* [1985] for comparable ice surfaces. At locations visually identified as dirty, spectral albedos were significantly lower, with a clear dependence on sediment loading.

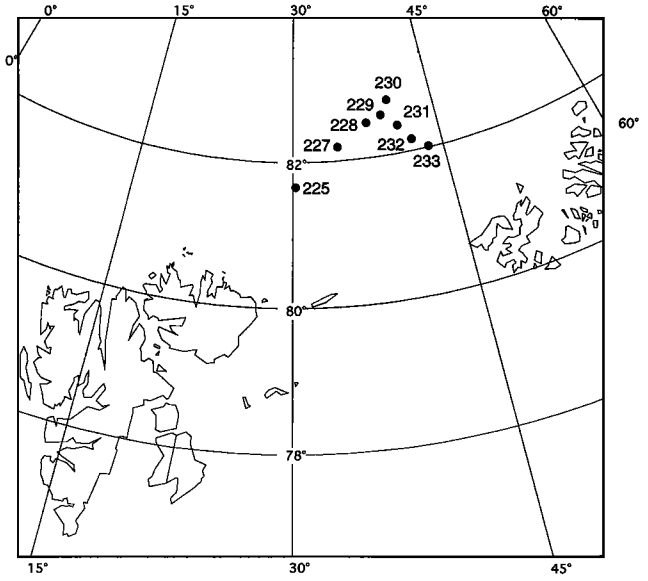

Figure 1. Map showing locations of spectral albedo and ice core measurements during the expedition ARCTIC 93 aboard the R/V *Polarstern* in August 1993. The sampling stations are denoted by their corresponding day of the year. Svalbard is the land mass on the left of the map.

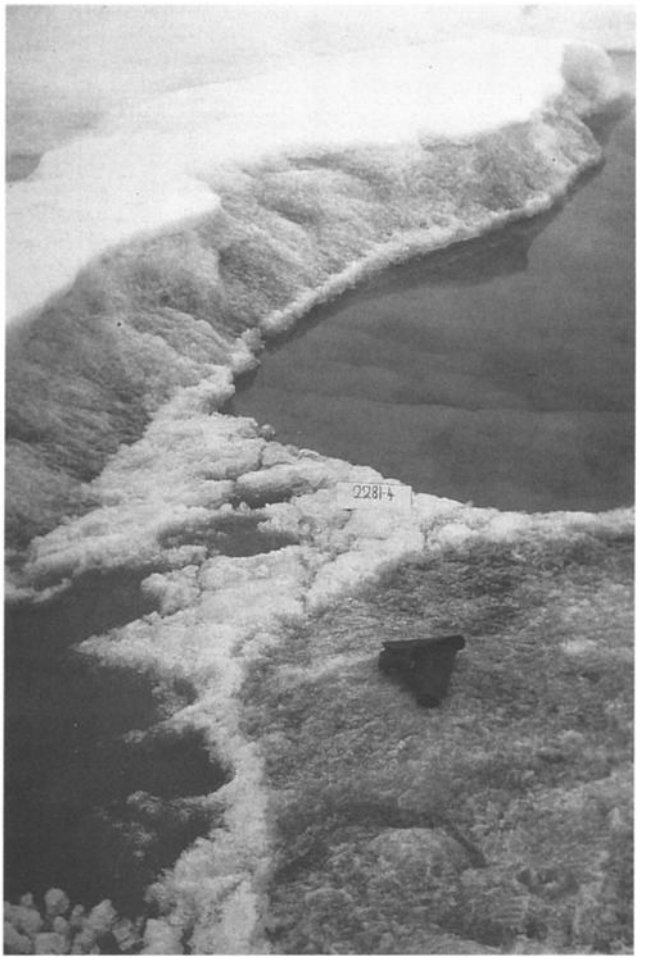

Figure 2. Photograph of multiyear ice with included sediment at station 228 (provided by E. Reimnitz). The ice was 2–3 m thick and covered by a thin layer of relatively clean deteriorated ice which appears white. Sediment particles can be seen in the layer beneath the surface scattering layer in the foreground and on the ice flanks above the melt pond. The pond surface (freeboard level) is ~21 cm below the ice surface.

Sediments were mostly concentrated in the upper few decimeters of the ice cover, with a distinct decrease in loading with increasing depth (see Figure 4). Despite high microstructural variability observed in the upper few decimeters of the ice [*Eicken et al.*, 1995], the vertical sediment profiles in multiyear ice were remarkably similar. Typically, maximum concentrations were found in the uppermost few centimeters of the ice with a steep decline in sediment loading with depth that reached background levels at roughly 0.5–1.0-m depth (see analysis of cores at high vertical resolution given by *Nürnberg et al.* [1994]). The low salinities and porous ice found at site C indicate that this distribution is a result of surface meltwater fluxes which redistribute and concentrate particulates near the ice surface, a location where the effect on ice albedo is most pronounced.

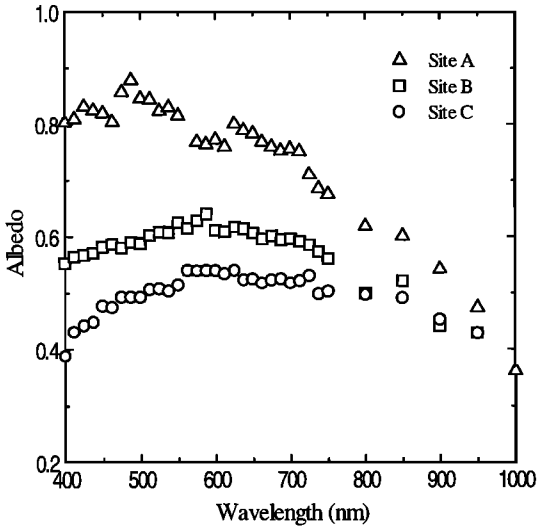

Figure 3. Measured spectral albedos of "clean" and particulate-laden sea ice. Site A (station 227 in Figure 1) was located at 82°12′N, 34°30′E and had ice that appeared clean to the observer. Site B (station 231, 82°23′N, 40°55′E) had ice with moderate particle loading (130 g m^{-3}). Site C (same location as site A) had ice with higher particulate loading (162 g m^{-3}). All three albedos were measured under overcast skies.

4. Modeling the Optical Properties of Particle-Laden Sea Ice

The objective of this work is to develop a more quantitative understanding of how particulates affect the optical properties of sea ice. To do this, we will first formulate a suitable treatment of absorption and scattering by particulates contained in dirty ice using field data and a four-stream, discrete-ordinates radiative transfer model. We will then utilize additional field data on spectral albedo and particulate loading to verify predictions made with the model. Finally, we will carry out sensitivity studies to assess the effects of particle size, type, concentration, and vertical distribution on the optical properties of the ice.

To describe radiative transfer in particle-laden sea ice, we used a structural-optical model [*Light*, 1995] coupled with a four-stream, multilayer radiative transfer model [*Grenfell*, 1991]. The structural-optical model takes information about the physical properties of the ice (e.g., composition and structure) and predicts inherent optical properties (absorption coefficient, scattering coefficient, and phase function) required by the radiative transfer model. The structural-optical model requires information about the vertical distribution of inclusions and utilizes equations of state developed by *Cox and Weeks* [1983] to predict relative volumes of air, brine, and solid ice. The radiative transfer model utilizes inherent optical properties, together with additional information about the boundary conditions, layer structure, and incident light field to solve the equation of transfer and predict apparent optical properties, such as the spectral albedo and transmissivity. The model assumes independent scattering by individual scatterers and represents the ice as locally plane-parallel. Vertical variations are approximated by multiple layers, each layer having uniform properties.

In the model, sea ice is treated as a matrix of pure ice with imbedded inclusions. The pure ice only absorbs light, while brine pockets, vapor bubbles, and particulates both scatter and absorb light. In general, relationships between the physical and optical properties of sea ice and its included inhomogeneities are described by separately specifying the absorption coefficient (κ) and scattering coefficient (σ) of each component in the system. By volume averaging the coefficients for each component, we get bulk values for κ and σ required by the radiative transfer model.

The bulk absorption coefficient for sea ice $\bar{\kappa}$ is the sum of spectral absorption coefficients for ice (subscript i), brine (subscript b), and particulates (subscript p),

$$\bar{\kappa}(\lambda) = \bar{\kappa}_i(\lambda) + \bar{\kappa}_b(\lambda) + \bar{\kappa}_p(\lambda) \quad (1)$$

Absorption by the ice and brine is assumed to depend only on their relative volumes; however, absorption by the included particulates depends on both volume and surface area of the particulate population, i.e., on their number and size distribution. Thus $\bar{\kappa}$ can be written as

$$\bar{\kappa}(\lambda) = \kappa_i(\lambda)V_i + \kappa_b(\lambda)V_b + \int_{r_{min}}^{r_{max}} \pi r_p^2 Q_{abs}^p(\lambda) N_p(r)\, dr \quad (2)$$

where V_i and V_b are the fractional volumes of ice and brine, respectively, $Q_{abs}^p(\lambda)$ is the spectral absorption efficiency for particulates, r_p is the particulate radius, $N_p(r)$ is the particulate size distribution, and λ is the wavelength. The value of $\kappa_i(\lambda)$ used in our calculations was taken from the experimental data of *Grenfell and Perovich* [1981] at wavelengths between 400 and 1000 nm (see Figure 5). For brine we used spectral absorption coefficients representative of natural arctic waters rather than values for highly purified laboratory water [e.g., *Pope and Fry*, 1997]. Values of $\kappa_b(\lambda) < 800$ nm were estimated using spectral data from *Smith and Baker* [1981] that were scaled to correspond with attenuation measurements at 490 nm made by *Smith* [1973] beneath Ice Island T-3 in the

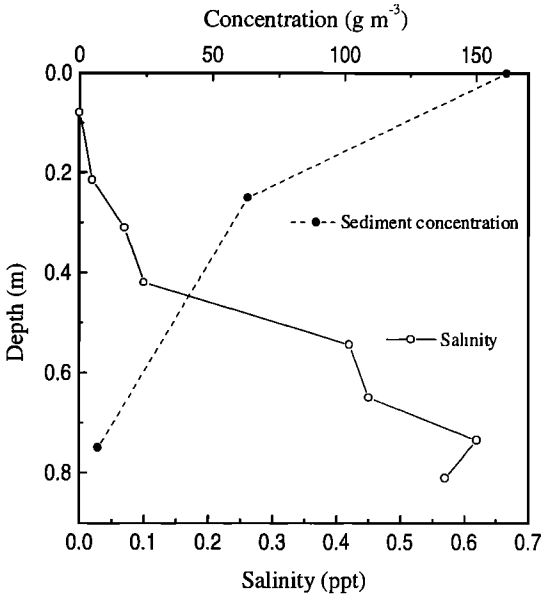

Figure 4. Vertical profiles of ice salinity and particulate concentration at site C. The ice above freeboard (21-cm depth) has a very low salinity and is highly porous. Note that the highest sediment concentrations at this site are found in the uppermost portions of the decomposed ice.

central Beaufort Sea. Data from *Irvine and Pollack* [1968] were used to describe $\kappa_b(\lambda)$ at wavelengths >800 nm (see Figure 5).

The bulk scattering coefficient for sea ice ($\bar{\sigma}$) is given by the sum of scattering coefficients for brine pockets, air bubbles (subscript a), and particulates:

$$\bar{\sigma} = \bar{\sigma}_b + \bar{\sigma}_a + \bar{\sigma}_p = Q^b_{sca}\pi r_b^2 N_b + \int_{r_{min}}^{r_{max}} Q^a_{sca}\pi r_a^2 N_a(r)\, dr + \int_{r_{min}}^{r_{max}} Q^p_{sca}\pi r_p^2 N_p(r)\, dr \quad (3)$$

In each case, the scattering efficiency Q_{sca} was computed using Mie theory and an appropriate size distribution $N(r)$. Since we lacked information on $N(r)$ for brine pockets, we assumed that the populations were monodisperse and based the number density on preliminary laboratory measurements [*Light*, 1995]. We also assumed that brine pockets and air bubbles are large enough that Q_{sca} is independent of wavelength, making $\bar{\sigma}$ also independent of wavelength.

The angular dependence of scattering for sea ice is given by the bulk phase function $\bar{p}(\theta)$ which is the following weighted sum of the phase functions for each component:

$$\bar{p}(\theta) = [\bar{\sigma}_b p_b(\theta) + \bar{\sigma}_a p_a(\theta) + \bar{\sigma}_p p_p(\theta)]/\bar{\sigma} \quad (4)$$

where θ is the scattering angle and $p_j(\theta)$ for each component j can be predicted by Mie theory. We assumed that all inclusions can be modeled as homogeneous spheres so that inclusion scattering characteristics may be determined using Mie theory. We approximated $p_j(\theta)$ with the Henyey-Greenstein function [*Henyey and Greenstein*, 1941] which relates $p_j(\theta)$ to its average cosine, the asymmetry parameter g_j,

$$p_j(\theta) = \frac{1 - g_j^2}{(1 + g_j^2 - 2g_j \cos\theta)^{3/2}} \quad (5)$$

Scattering coefficients and the phase function for the Mie solution are related to the size and composition of spherical particles through a size parameter $x = 2\pi r/\lambda$ and a complex index of refraction $m = n - ik$, where the real part n is the ratio of the speed of light in a vacuum to its speed within the inclusion and the imaginary part k is an absorption parameter. The real and imaginary refractive indices along with the particle size parameter x were used with Mie calculations to predict Q_{abs}, Q_{sca}, and g_j [see *Evans*, 1988].

5. Comparison of Theory and Observation

In this section we will formulate and test a method to predict how particulates affect radiative transfer in sea ice. The structural-optical model will first be used to infer ice properties at the clean ice site. These properties will then be used to test predictions of optical properties at particle-laden sites.

5.1. Ice Properties

We first need to establish an ice structure to be used in the structural-optical model. To do this, we require specific information on the physical properties of the ice, including vertical profiles of temperature, salinity, density, and structure. With such information, the structural-optical model can predict inherent optical properties for the ice. Observations made at the field sites provide the basis for estimating the ice properties.

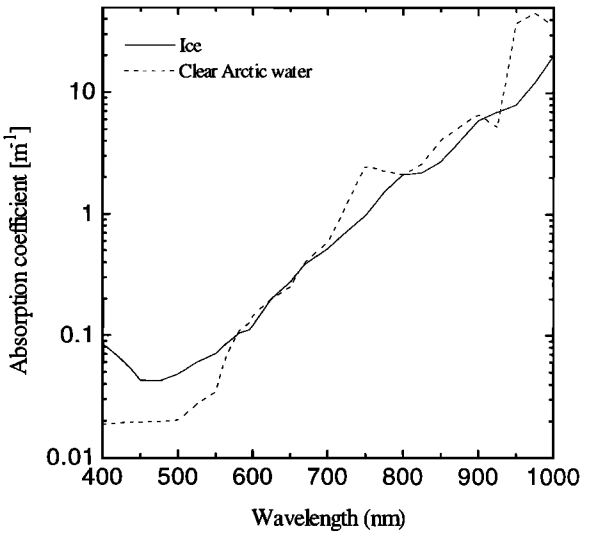

Figure 5. Spectral absorption coefficients for pure ice and clear Arctic water based on data from *Smith* [1973], *Smith and Baker* [1981], and *Grenfell and Perovich* [1981].

Ice at the measurement locations shared several common physical characteristics. In all cases it was thick, melting multiyear ice with similar vertical structure. The structure typically consisted of a thin, granular, highly scattering layer at the surface, an intermediate layer with low density and enhanced air volume, and a thick bottom layer of warm ice having a significant brine volume. This general pattern appears to be typical of melting, multiyear ice in the Arctic. For this reason, we chose to represent the structure of the ice with a three-layer model.

Field data indicate that the deteriorated upper layer typically has a density of ~500 kg m^{-3}, a salinity of 0 parts per thousand (ppt), and a thickness of ~0.05 m. These values were used to characterize the upper layer in model calculations. Because of its granular texture and absence of brine, we chose to model this upper layer as a mixture of loosely packed, spherical ice grains and particulates surrounded by air. As a result of the absence of inclusions of brine or air bubbles in the ice grains, (2), (3), and (4) reduce to

$$\bar{\kappa}(\lambda) = \pi r_g^2 Q^g_{abs}(\lambda) N_g + \int_{r_{min}}^{r_{max}} \pi r_p^2 Q^p_{abs}(\lambda) N_p(r)\, dr \quad (6)$$

$$\bar{\sigma} = \bar{\sigma}_g + \bar{\sigma}_p = Q^g_{sca}\pi r_g^2 N_g + \int_{r_{min}}^{r_{max}} Q^p_{sca}\pi r_p^2 N_p(r)\, dr \quad (7)$$

$$\bar{p}(\theta) = [\bar{\sigma}_g p_g(\theta) + \bar{\sigma}_p p_p(\theta)]/\bar{\sigma} \quad (8)$$

where the subscript g represents quantities defined for ice grains. Assuming the ice grains to be spherical, their number density is given by

$$N_g = \frac{3}{4\pi r_g^3}\frac{\rho}{\rho_i} \quad (9)$$

where ρ is the density of the deteriorated layer and ρ_i is the density of pure ice. The ice grain population was assumed to be monodisperse with $r = 2.5$ mm. Mie theory was then used to calculate $Q_{abs}(\lambda)$, Q_{sca}, and g.

Despite efforts to quantify the physical properties of the

Table 1. Assumed Physical and Inherent Optical Properties for the Clean Ice Observed at Site A

Layer	Thickness, m	Physical Properties	$\bar{\sigma}$, m^{-1}	$\bar{\kappa}$, m^{-1}	$\bar{g}$
1	0.05	R_g = 2500 μm, ρ_i = 500 kg m^{-3}	327	0.03338	0.89
2	0.20	V_b = 0.02, V_a = 0.20 R_b = 90 μm, R_a = 600 μm	730	0.03450	0.90
3	2.60	V_b = 0.10, V_a = 0.02, R_b = 430 μm, R_a = 120 μm	480	0.03930	0.92

Optical properties given are for wavelength of 500 nm. These values were also used for the analysis of data from sites B and C.

lower layers of the ice, we lacked detailed information about the microstructure of the ice, specifically estimates of the number distribution and effective size of inclusions of air and brine. We were thus unable to formulate accurate predictions of κ and σ for these layers based strictly on information about ice temperature, salinity, and density. Instead, we initially selected values for V_a, V_b, and r_a that seemed reasonable on the basis of previous observational work [e.g., *Weeks and Ackley*, 1986]. The middle layer was assumed to be 20 cm thick with V_b = 2% and V_a = 20%. The thickness of the third layer was assumed to be 260 cm with V_b = 10% and V_a = 2%. *Perovich and Gow* [1996] observed that melting first-year ice contained ~5 brine pockets per mm^3, and this value was initially adopted for use in these calculations. In both layers, the effective air bubble radius (R_a) was set to 1.3 mm on the basis of observations by *Grenfell* [1983].

These quantities were initially used with the model to try and match observed spectral albedos at the clean ice site (site A). While there was general agreement between observed and predicted values, it was evident that tuning N_b and R_a (both of which have a high degree of uncertainty) could produce even better agreement. Values that produced the best agreement were R_a = 0.60 mm and N_b = 5 mm^{-3} for the above-freeboard layer and R_a = 0.12 mm and N_b = 0.2 mm^{-3} in the lowest layer. These values suggest that the effective size of brine pockets in the lowest layer was larger than that in the middle layer (430 μm as opposed to 90 μm), but brine pockets in the lowest layer were fewer in number (0.2 mm^{-3} as opposed to 5 mm^{-3}). While physically plausible, there are no actual data to support these numbers. It is not, however, the physical properties that are important to this analysis but rather the bulk optical properties ($\bar{\sigma}$, $\bar{g}$, and $\bar{\kappa}$) implied by the physical properties (see Table 1). Values of $\bar{\sigma}$, $\bar{g}$, and $\bar{\kappa}$ shown in Table 1 produce close agreement with the albedo observations at site A; however, they could have been generated using a different set of V_b, V_a, N_b, N_a, R_b, and R_a values.

Figure 6 shows the observed albedo at site A, along with the theoretical prediction from the three-layer clean ice model. Overcast conditions were simulated using isotropic incident radiation with spectral characteristics given by *Grenfell* [1979]. The predicted albedo is larger than that observed when $\lambda <$ 800 nm and smaller at longer wavelengths. While it is possible to adjust the predicted albedo by altering the optical properties of the ice, this does not produce significantly better agreement with the observations. For example, decreasing the scattering would improve the agreement at short wavelengths but would make it worse at long wavelengths. Likewise, because of the similarity between κ_i and κ_b, there is no practical way to substantially alter the bulk absorption coefficient without the addition of material with distinctly different absorption properties. The possibility that foreign material was present in the supposedly clean ice is supported by nearby measurements which indicate 5–10 g m^{-3} of particulates in ice that appeared clean to the eye. We suspect that trace concentrations of particulates and possibly dissolved material in this clean ice were responsible for much of the discrepancy between the observations and theoretical predictions at visible wavelengths. In sections 5.2 and 5.3, we will examine this hypothesis.

5.2. Inherent Optical Properties of Sediment Particles

Lacking data on the amount of dissolved material in the ice, we will assume for purposes of this study that the albedo discrepancy is due strictly to the presence of sediment particles. Unfortunately, the optical properties of these sediments have yet to be determined. Measurements of light absorption by detritus contained in sea ice have been made [*Roesler et al.*, 1989; *Roesler and Iturriaga*, 1994], and, although such detritus is likely to include sediment particles, it is not clear whether these absorption values provide a suitable description of material that is composed primarily of sediments. This question can be examined using the field data and radiative transfer model. With suitable assumptions about the effective size (R_p) and complex refractive index [$n_p(\lambda) - ik_p(\lambda)$] of the particulates, it is possible to estimate an effective $\bar{\kappa}_p$, $\bar{\sigma}_p$, and $\bar{g}_p$ using Mie theory. These quantities, along with those in Table 1,

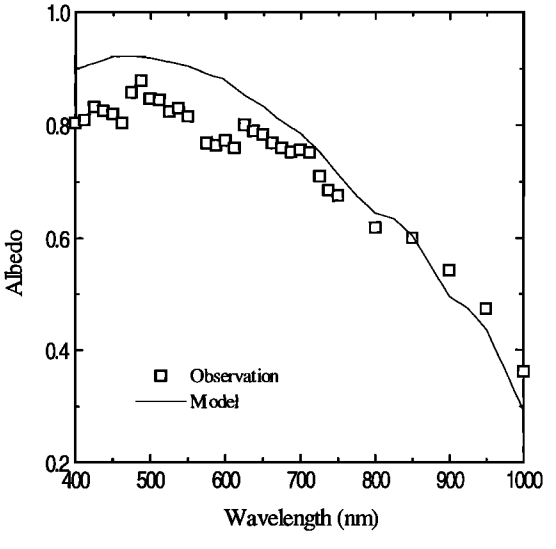

Figure 6. Measured and modeled albedos for ice assumed to be clean (site A).

allow us to determine the bulk properties needed for the prediction of spectral albedo. In this section, we will derive estimates of R_p, $n_p(\lambda)$, and $k_p(\lambda)$.

Reimnitz et al. [1993] used sieve and pipette analyses to estimate the size distribution of sediment contained in ice from the Beaufort Sea. They reported that ~51% of the particle mass was clay ($r_p < 2$ μm), 47% was silt (2 μm $< r_p <$ 31 μm), and 2% was sand (31 μm $< r_p <$ 1 mm). Similar findings by *Nürnberg et al.* [1994] give 49% clay, 40% silt, and 11% sand in the Central Arctic. The smallest particles appeared to be ~0.5 μm in radius. Given such crude information about the size distribution, we will estimate R_p by establishing lower and upper limits on particle size and assuming an analytic form for the size distribution, $N(r)$. Following *Hansen and Travis* [1974],

$$R_p = \frac{\int_{r_{min}}^{r_{max}} r^3 N(r)\, dr}{\int_{r_{min}}^{r_{max}} r^2 N(r)\, dr}. \quad (10)$$

To describe the sediments, we chose a convenient power law distribution, $N = N_0 r_p^{-m}$, where the best fit to the observations of *Nürnberg et al.* [1994] was obtained with $m = 4.4$. With regard to the upper limit of particle size, we used the radiative transfer model to test the effect of sand-sized particles on albedo and found that their impact is negligible when their fractional mass is small compared to the total mass of clay and silt particles. Since the observations indicate a dominance of silt- and clay-sized particles, we can ignore the sand and restrict our attention to particles with $r_p < 31$ μm. Assuming size limits of 0.5 and 31 μm, (10) yields an R_p close to 3 μm.

Real and imaginary refractive index data have been reported for a variety of mineral dusts and aerosols of different composition. Observations of *Zaneveld et al.* [1974] indicated that average n values are close to 1.54 at visible wavelengths for oceanic particles composed of either inorganic material or organic skeletal material. *Patterson et al.* [1977] measured Saharan aerosol and found representative values of n to be 1.558 at 550 nm and 1.552 at 633 nm. *Grams et al.* [1974] found airborne soil particles at a rural semi-arid location to have a typical value of 1.525. Work reported by *Carlson and Benjamin* [1980] suggest that n for Saharan and other soil-derived aerosols varies between 1.54 and 1.58 in the wavelength interval between 320 and 690 nm. For the most part, however, such small variations in n will have little effect on scattering, particularly when there is high particulate absorption, so we assumed that $n = 1.54$ at all wavelengths.

Although n is independent of wavelength, we do not expect this to be the case with k. For example, because of their red-brown appearance, we expect sediment particles to absorb more blue light than red light. Measurements of spectral absorption by soil-derived particulates suspended in the atmosphere have been carried out by several investigators. *Patterson et al.* [1977] report measurements of $k(\lambda)$ for Saharan and other lithogenic aerosols, which show decreasing values from 0.02 at 300 nm to 0.004 at 700 nm. *Carlson and Caverly* [1977] found $k(\lambda)$ for Saharan dust to be 0.018 at 375 nm, 0.008 at 468 nm, and 0.0029 at 610 nm. *Carlson and Benjamin* [1980] report a collection of complex spectral refractive indices for Saharan and desert aerosol, showing absorption minima at ~650 nm and ranging in value from 0.001–0.04 at visible wavelengths. *Grams et al.* [1974] made numerous measurements of $k(\lambda)$ at 500 nm for soil-derived aerosol and found an average value of ~0.005. *Lindberg and Laude* [1974] measured $k(\lambda)$ for desert dust in New Mexico and obtained values of 0.010 at blue wavelengths, decreasing to 0.006 at red wavelengths. These data typically show a strong spectral gradient in the blue, minima around 600 nm, and increased values at longer wavelengths. We expect these materials to be somewhat similar to sediment particles entrained in sea ice, but no direct comparisons have yet been made.

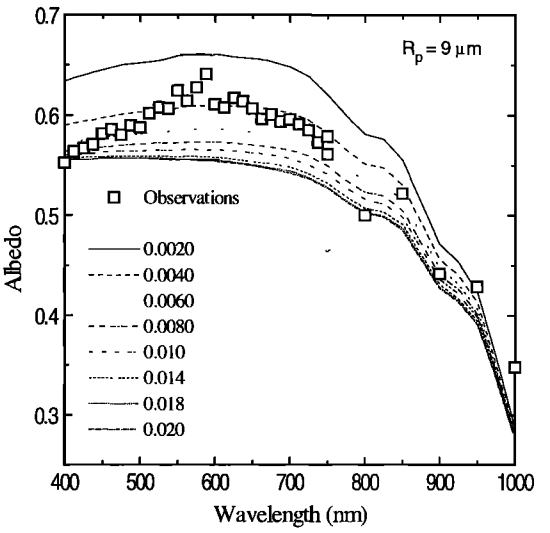

Figure 7. Theoretical values of spectral albedo for 9 μm particles entrained in the ice are shown for eight different values of k_p between 0.002 and 0.02. These albedos were used to infer $k_p(\lambda)$ by superimposing them on the measured spectral albedo at site B (squares) and choosing values of $k(\lambda)$ where theory and observation coincided.

Lacking direct measurements of $k_p(\lambda)$ and R_p for sediment particles in sea ice, we inferred them jointly using our model and the spectral albedo observations from site B. Our overall approach was to select a particular value of R_p and then generate predictions of spectral albedo, $\alpha(\lambda)$, for 16 different values of k which we expect to span the true value. Specifically, we (1) calculated Mie parameters (Q^p_{sca}, $Q^p_{abs}[\lambda]$, g) for the particulates using a broad range of R_p and k values, (2) used (2)–(4) to calculate depth-dependent bulk optical properties at site B by specifying observed particulate loading in each layer of the clean ice model, and (3) incorporated these bulk properties into the radiative transfer model to obtain a set of theoretical $\alpha(\lambda)$ values for different R_p and k values. The set of $\alpha(\lambda)$ predictions was then superimposed on the albedos observed at site B (see Figure 7). The k value needed to match predictions with observations at specific wavelengths was then taken from the graph at 50 nm intervals to infer $k_p(\lambda)$ for the chosen R_p (see Figure 7). The procedure was repeated for additional values of R_p to find the $k_p(\lambda)$ that most closely matched the available spectral absorption information. In each case we assumed that $n = 1.54$ for the particulates and 1.31 for the ice.

Observations at site B indicated that sediment concentration was low in the uppermost 1 cm of the ice with large, but relatively constant, values down to the freeboard level. Ice below this again appeared to be relatively clean. To model this distribution, we assumed that 5 g m^{-3} of particulates were

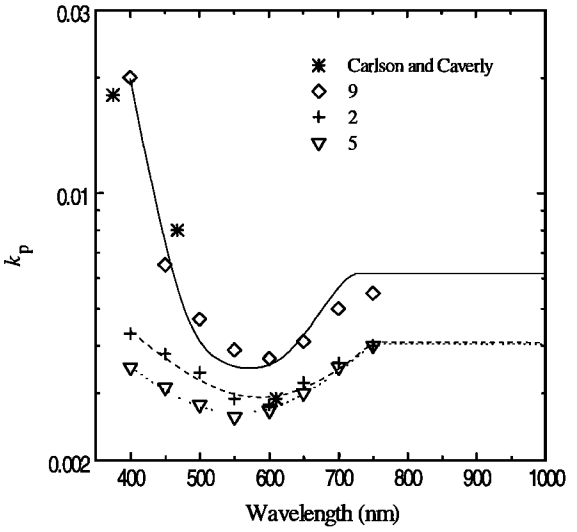

Figure 8. Inferred $k_p(\lambda)$ values for three different particle sizes (2, 5, and 9 μm). Observations of *Carlson and Caverly* [1977] are shown as asterisks. The three lines represent the corresponding parameterized fits used in the radiative transfer model.

contained in the top 1 cm of the ice, with 136 g m^{-3} down to the freeboard level and no particulates in the lowest layer. Values of $k_p(\lambda)$ derived from three values of R_p (2, 5, and 9 μm) are shown in Figure 8. Also shown are values for Saharan aerosol [*Carlson and Caverly*, 1977]. The $k_p(\lambda)$ obtained when $R_p = 9$ μm is most similar to the Saharan aerosol values, both in magnitude and in spectral shape. We believe the $k_p(\lambda)$ values for $R_p = 9$ μm provide an acceptable characterization of absorption by sediment particles in sea ice. Inferred values of $k_p(\lambda)$ for $R_p = 9$ μm were then fit to a 5th-order polynomial for use in the radiative transfer model,

$$k_p(\lambda) = 4.31 - (3.62 \times 10^{-2})(\lambda) + (1.22 \times 10^{-4})(\lambda^2) - (2.04 \times 10^{-7})(\lambda^3) + (1.71 \times 10^{-10})(\lambda^4) - (5.69 \times 10^{-14})(\lambda^5) \qquad 400 \le \lambda < 730 \text{ nm} \quad (11)$$

$$k_p(\lambda) = 0.00618 \qquad \lambda \ge 730 \text{ nm}$$

where λ is in nanometers. This function is plotted as the solid line in Figure 8 and will be used in subsequent calculations to describe light absorption by sediment particles in sea ice. Above 730 nm, uncertainties in the measured albedos precluded reliable estimates of $k_p(\lambda)$, so the value at 730 nm was simply assumed to also describe absorption at longer wavelengths. Because ice dominates the absorption at these wavelengths, this assumption should have minimal impact on the predicted albedos.

It appears from these results that the effective size of sediment particles contained in the ice is of the order of 9 μm. However, this is considerably larger than the 3 μm estimated from the measured particle size categories and assumed power law distribution. The reason for this may be that the measurements are biased toward smaller particles since the experimental procedure involved filtering, rinsing, and sorting which could have destroyed some natural, in situ aggregation. Thus it seems likely that the actual value of R_p is larger than that derived from the power law distribution. An effective size of 9 μm corresponds to an exponent of 3 in the power law distribution and indicates that most of the sediment mass is fine silt.

5.3. Albedo Comparisons

In the preceding section, we derived values for $k_p(\lambda)$ and R_p which, when used with the radiative transfer model, allowed us to closely match the observed $\alpha(\lambda)$ at site B. To test the general applicability of these values, we next applied the model at site C where the sediment concentrations were significantly larger. The observations indicate that sediment loading at site C was relatively constant with depth above the freeboard level. With values of $k_p(\lambda)$ and R_p from site B, model predictions of $\alpha(\lambda)$ at site C were in excellent agreement with the observations (Figure 9) when sediment loading above the freeboard level was 170 g m^{-3}, a number very close to the amount measured.

In section 5.1 we speculated that differences between observed and predicted $\alpha(\lambda)$ values for clean ice were due to the presence of trace quantities of particulates or dissolved material in the ice. To determine the concentration of particulates needed to account for this difference, particles with the same properties as the sediments were introduced into the uppermost 0.25 m of the model. Excellent agreement between predictions and observations was obtained at the apparently clean site (site A) when a particulate concentration of 8 g m^{-3} was used (Figure 9). Concentrations this low would not be noticed with the eye but are sufficient to reduce spectral albedos by 5–10% at visible wavelengths. This suggests that there is a background level of contaminant loading in the upper part of the arctic ice pack of the order of 5–10 g m^{-3}. While sediment particles may contribute to this loading, much of it is likely due to deposition of dust, soot, and other pollutants transported by the atmosphere, as well as to dissolved matter and biogenic material such as microalgae.

The results presented in Figure 9 provide strong support for our treatment of the effects of particulate inclusions on radiative transfer in sea ice at wavelengths below 800–850 nm. At longer wavelengths, however, the model consistently underes-

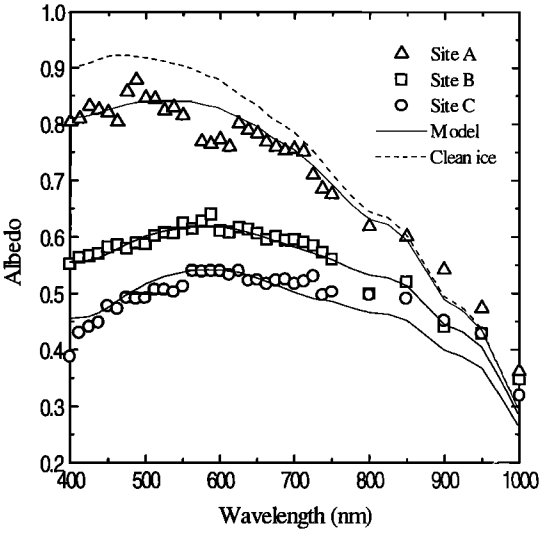

Figure 9. Comparison of observed and predicted spectral albedos for sites A, B, and C. Solid lines show corresponding model predictions, and the dashed line shows the albedo predicted by the model for the same ice with no particulates.

timates $\alpha(\lambda)$ at all sites. Although an overestimation of $k_p(\lambda)$ or measurement errors could contribute to this, the most probable explanation is that we have included insufficient structural detail in our model of the uppermost layer of the ice. At wavelengths longer than 800 nm, absorption by the ice begins to dominate $\bar{\kappa}(\lambda)$, while $\alpha(\lambda)$ becomes increasingly sensitive to such things as vertical gradients in grain size and density and less sensitive to particulate loading. Because our focus is on the particulates, we have not attempted to increase the vertical complexity of the upper layer in order to match albedos at longer wavelengths. Nevertheless, we believe that the present model adequately treats the effects of particulates on the radiation field. In section 6, we will utilize this model to examine how the properties and distribution of the included particulates affect $\alpha(\lambda)$.

6. Sensitivity Studies

It is reasonable to expect that differences in ice growth rates, current speeds, water depth, and other environmental factors will affect the concentration profile and size distribution of sediment particles entrained within the ice. Also, there are likely to be optical and compositional differences between sediment particles and those derived from atmospheric deposition or from biological activity. In this section we will examine how such variations impact $\alpha(\lambda)$. To avoid complicating the interpretation of results, we will use ice with drastically simplified vertical structure and optical properties for these sensitivity tests. Such ice is, of course, not found in nature but provides a simple medium in which the relative effects of particulate variations can be quantified.

For these studies, we chose ice with a 1 cm thick deteriorated layer on top of 2.84 m of ice with uniform brine volume (V_b = 0.10), uniform air volume (V_a = 0.02), and uniform air bubble radius (r_a = 0.12 mm). These two layers have properties identical to the uppermost and lowermost layers of the model analysis of the field measurements. While we are not attempting to simulate multiyear ice exactly, the predicted response of $\alpha(\lambda)$ to particulate variations should be comparable in magnitude to those that would occur over multiyear ice. Specific variations we will discuss in this section include particle concentration, vertical distribution, size, and composition.

6.1. Particulate Concentration

To examine how $\alpha(\lambda)$ responds to changes in the concentration of particulates, a 10 cm thick layer of contaminated ice was placed 1 cm below the surface, and its particle concentration was varied between 0 and 1000 g m^{-3}. Figure 10a shows how the albedo varies with wavelength and concentration. As the concentration increases, the albedo at each wavelength decreases. These changes are larger at visible wavelengths than at longer wavelengths because absorption by the ice becomes increasingly dominant as wavelength increases, reducing the relative importance of absorption by the particulates. An albedo maximum occurs at the wavelength of minimum $\bar{\kappa}(\lambda)$. For clean ice this occurs at 470 nm but shifts toward longer wavelengths as particulate loading increases and alters the spectral shape of $\bar{\kappa}(\lambda)$ in the visible. There is an inverse correlation between particle loading and spectral albedo gradients in the red and near-infrared parts of the spectrum. This is due to the rapid increase in $\kappa_i(\lambda)$ with wavelength, in combination with the decrease of $\kappa_p(\lambda)$ in this wavelength region. The decrease in albedo with concentration is shown in Figure 10b

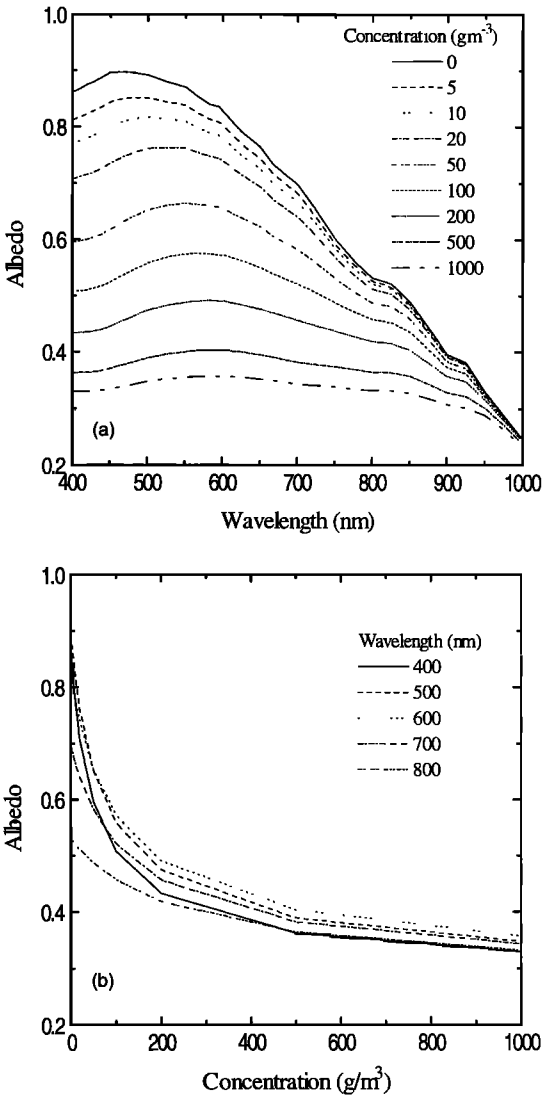

Figure 10. Sensitivity of spectral albedo to particulate concentration: (a) albedo as a function of wavelength for various particulate concentrations (g m^{-3}) and (b) albedo as a function of concentration for specific wavelengths (nanometers). The effective radius of the particulates was held constant at 9 μm, as was the 10 cm thickness of the particulate-bearing layer which was located at a depth of 1 cm below the ice surface.

at selected wavelengths. It is evident that $\alpha(\lambda)$ responds most sensitively to changes in particulate loading when concentrations are small and that this response rate is greatly reduced when concentrations exceed 100–200 g m^{-3}.

6.2. Vertical Distribution of Particulates

We next examine how the thickness and depth of a sediment-bearing layer affects $\alpha(\lambda)$. In each case, particle size (R_p = 9 μm) and concentration (100 g m^{-3}) were held constant. Changes in layer thickness are therefore accompanied by changes in total particulate mass. In Figure 11a, predicted albedos are shown as a function of wavelength and layer thickness, assuming the top of the layer to be fixed 1 cm below the surface. The presence of a 1-cm thick layer of particulates substantially decreases the albedo relative to that of clean ice. However, once the layer thickness reaches about 10 cm, further increases in thickness have minimal impact on the albedo.

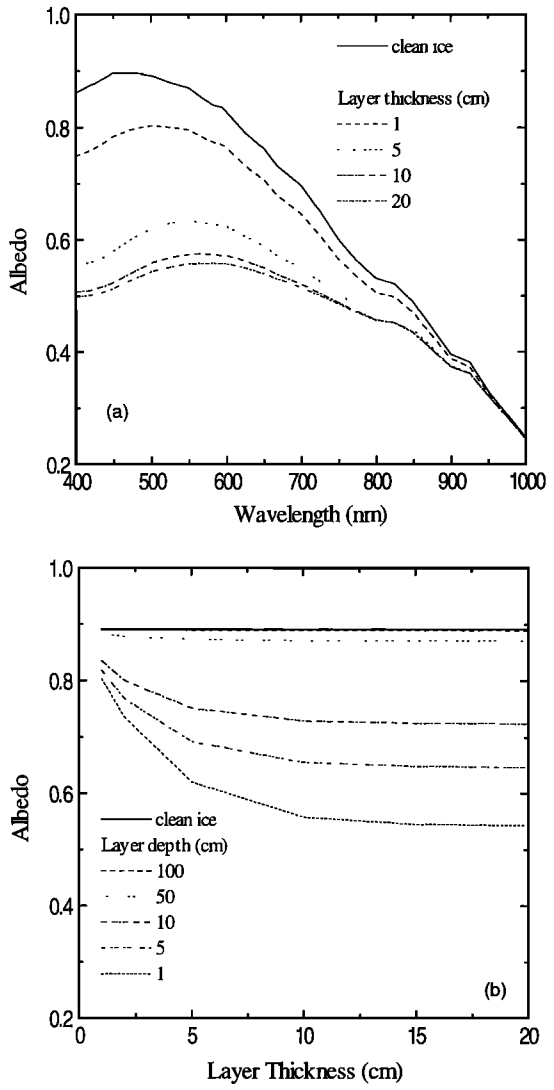

Figure 11. Sensitivity of albedo to depth and thickness of a particulate-laden layer within the ice. (a) Albedo as a function of wavelength and layer thickness for a particle-laden layer beginning 1 cm below the surface is shown. Layer thickness is identical to total loading in g m^{-2}. (b) Albedo at 500 nm where the depth and thickness of the layer were varied over the ranges 0–1.0 m and 0–0.20 m, respectively, is shown. In each case, the particle concentration was held constant at 100 g m^{-3} and the effective particle radius was 9 μm.

This is because little of the backscattered light penetrates below 10 cm because of large attenuation in the surface layers. Had particle concentration been higher, this depth would have been even <10 cm.

Figure 11b shows how the albedo changed when both the thickness and depth of the contaminated layer were varied. Values are shown at λ = 500 nm, the region of minimum bulk absorption and maximum light penetration for moderate particulate loading. The results show that a particulate layer has little effect on $\alpha(\lambda)$ if it is covered by more than ~50 cm of ice, and layer thickness has essentially no effect on albedo if the sediment layer begins deeper than 20–30 cm below the surface. The lowest albedos are, of course, produced by thick layers that start near the surface. Changes in layer thickness affect the albedo most strongly when the layer is near the surface, and changes in layer depth affect the albedo most strongly when the layer thickness is large. As layer thickness increases, increased absorption reduces the amount of backscattered light and the magnitude of $\alpha(\lambda)$. At some point, absorption saturates and the optical properties of the lower portions of the layer, along with the ice below it, do not affect $\alpha(\lambda)$. The general shape of these curves is similar at other wavelengths except that saturation occurs for thinner layers and shallower depths.

6.3. Particle Size

Particle size is an important parameter because, for a given mass of particulates, the total surface area of the population decreases as R_p increases. This decreases the total scattering and, if the value of k_p is sufficiently large (as it is for these particles), also decreases the total absorption. Since absorption and scattering are both sensitive to particle size and since there is some uncertainty in our estimate of R_p, we will examine the effects of particle size on albedo. Again, the particulates are contained in a 10-cm thick layer 1 cm below the surface with a fixed concentration of 100 g m^{-3}.

Figure 12 shows the albedo at five wavelengths as a function of R_p. For $\lambda \geq 500$ nm, particle size has only a small effect on $\alpha(\lambda)$ as long as 1 μm $\leq R_p \leq$ 5 μm. This is because larger particles contain a significant amount of mass in their interior which is shielded from the radiation field and does not participate in absorption, a process we call "self-shading." The degree of self-shading depends on the optical thickness of the particle which, in turn, depends on the product of R_p and $k_p(\lambda)$. At wavelengths above ~500 nm, an increasing fraction of the total particulate mass is shaded as R_p grows beyond 5 μm, causing bulk absorption to decrease and albedo to increase. At shorter wavelengths, particles as small as 1 μm can be optically thick because of the increased value of k_p with decreasing wavelength (see Figure 8). This means that $\alpha(\lambda <$ 500 nm) becomes increasingly sensitive to R_p as wavelength

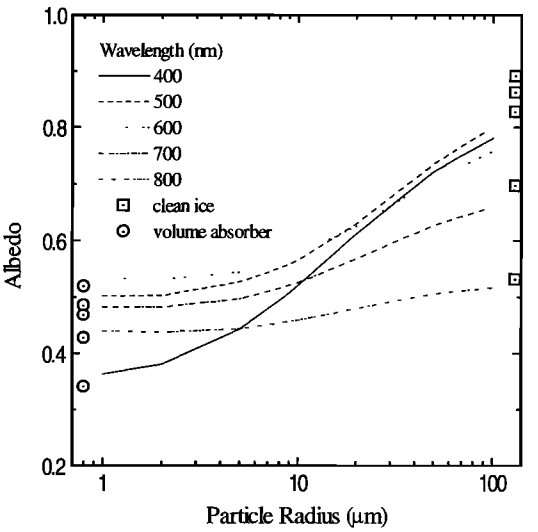

Figure 12. Albedos at five wavelengths (nanometers) as a function of effective particle radius. The particulates are contained in a 10-cm thick layer beginning 1 cm below the surface of the ice and have a fixed mass concentration of 100 g m^{-3}. Corresponding albedos for clean ice are indicated by squares, and those where the particulate material is treated as a simple "volume-absorber" are indicated by circles.

decreases. When the particles become very small ($R_p \ll 1$ μm), there is no self-shading effect, and they become pure "volume absorbers" where the albedo depends only on the total mass of the particulates and on the wavelength. Albedo values for volume absorbers are indicated by open circles in Figure 12. It can be seen that albedos for $R_p = 1$–2 μm are within a few percent of the volume-absorber limit.

As might be expected from earlier simulations, the effect of particle size on albedos at $\lambda \geq 800$ nm is relatively small because of high absorption in the surrounding ice. In general, the albedo begins to approach that of clean ice when $R_p = 100$–200 μm. This is due to a reduction in the number and surface area of the particulates and to the increased importance of self-shading. The most important conclusion to be drawn from these studies is that the effective size ($R_p = 9$ μm) of the particulates at the experimental sites (see section 5) is much larger than the volume-absorber limit and that estimates of particulate loading cannot be obtained from $\alpha(\lambda)$ data without knowing R_p.

6.4. Comparisons With Other Types of Particulates

In addition to sediments, substantial amounts of atmospheric dust, soot, and algae can be present in the upper layers of the ice. To compare the effects of other types of particles on $\alpha(\lambda)$, we first identified typical concentrations which were then used to evaluate the $\bar{\kappa}_p(\lambda)$ in (1). Algae concentrations were taken from *Gradinger and Nürnberg* [1996], who reported values of chlorophyll *a* in excess of 0.05 g m^{-3} at the surface of multiyear ice. Soot concentrations were taken from *Warren* [1982], who found that 0.15 ppt of soot (0.135 g m^{-3} in sea ice) was needed to explain snow albedos taken at Ice Island T-3 in the Central Arctic Ocean. For purposes of comparison, sediment and atmospheric dust particles were assumed to have identical optical properties and to have a concentration of 100 g m^{-3}. Values of $\bar{\kappa}_p(\lambda)$ for sediments were calculated as before. For soot, $\bar{\kappa}_p(\lambda)$ was calculated using results of Mie calculations by S. G. Warren (personal communication, 1993), assuming an $R_p = 0.13$ μm and a complex refractive index of 2.0–i0.66 that was independent of wavelength. In the case of the algae, $\bar{\kappa}_p(\lambda)$ was computed from the chlorophyll concentration and relative spectral absorption coefficients determined empirically by *Soo Hoo et al.* [1987].

Results of these calculations and those for pure ice are shown in Figure 13a. In the visible, it is clear that particulates are the dominant absorbers, ice and brine pockets being of secondary importance. Above about 750 nm, however, absorption by ice and brine increases rapidly and overwhelms the particulate absorption. While soot is close to being a "grey absorber" that absorbs light equally at all wavelengths, algae have strong absorption peaks around 435 and 670 nm and no appreciable absorption above ~720 nm. Absorption by dust and sediment particles decreases fairly rapidly in the visible to a minimum at ~600 nm, like the algae. If our assumptions are correct, however, absorption by the sediments remains fairly high throughout the near infrared.

Figure 13b shows how these different types of particulates affect $\alpha(\lambda)$, again assuming that they are uniformly distributed in a 10-cm thick layer beginning 1 cm below the surface. Although the absolute degree to which albedo is reduced depends on assumed particle concentration, there are clear differences in the spectral response to different particle types. Both soot and sediment alter the spectral gradient of $\alpha(\lambda)$ in the near infrared, while algae have little effect beyond 650–700 nm. In the visible, sediment tends to absorb more energy in the blue than soot but less energy at green to red wavelengths. Location of the albedo maximum (α_{max}) provides the best indication of the type of particulates present. The α_{max} for clean ice occurs at around 470 nm and at ~600 nm for algae-contaminated ice, unless the concentration is less than ~0.04 g m^{-3}. For soot and sediments, there is a direct relationship between the location of α_{max} and concentration, where α_{max} of soot occurs between 400 and 470 nm and α_{max} of sediments occurs between 470 and 600 nm regardless of ice type. However, efforts to infer particulate loading from $\alpha(\lambda)$ data alone would again be complicated by uncertainties in particle size and vertical distribution.

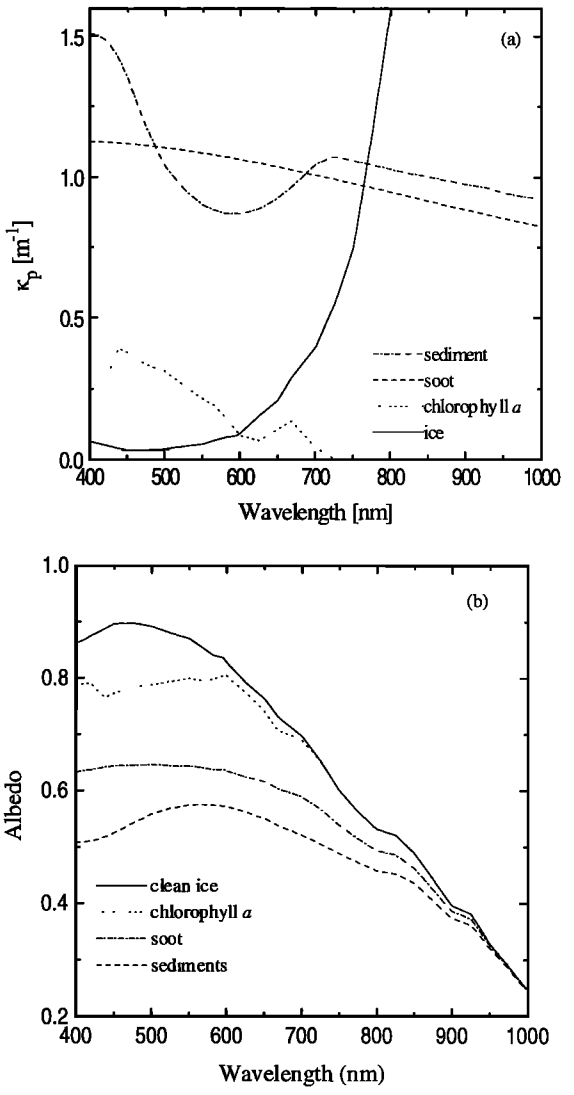

Figure 13. Effects of carbon soot, chlorophyll *a*, and sediments on (a) $\bar{\kappa}_p(\lambda)$ and (b) spectral albedo. The concentrations were set to 0.135 g m^{-3} for carbon soot, 0.05 g m^{-3} for chlorophyl *a*, and 100 g m^{-3} for the sediment. In Figure 13a, the value of $\kappa(\lambda)$ for pure ice is also shown for comparison. In Figure 13b, each contaminant was evenly distributed within a 10-cm thick layer 1 cm below the ice surface.

7. Discussion

The presence of particulates clearly impacts the radiative balance of sea ice. In addition to sediments entrained by young

ice in the shelf regions, significant amounts of dust, soot, algae, and dissolved material can also be present in the ice. Because biological processes tend to be most vigorous near the bottom of the ice in the Arctic, algal cells primarily affect the transmission of light to the ocean. In contrast, sediments, dust, and soot tend to be concentrated in the upper part of the ice, affecting not only transmission but also the absorption and reflection of shortwave energy by the ice. Our analysis indicates that even ice observed to be clean is likely to contain trace quantities (5–10 g m^{-3}) of particulates which reduce albedos at visible wavelengths by 5–10% (Figure 9), in accord with field measurements indicating background particle concentrations in clean sea ice of a few g m^{-3} [*Reimnitz*, 1994; *Nürnberg et al.*, 1994; *Eicken et al.*, 1997]. These albedos are comparable in magnitude and spectral shape to earlier albedo measurements [e.g., *Grenfell and Maykut*, 1977; *Maykut and Perovich*, 1985], suggesting that the ice in these previous studies may also have contained small amounts of particulates.

The excellent agreement between observed and predicted albedos of sediment-laden ice demonstrates that the structural-optical ice model, when used in combination with the four-stream radiative transfer model, provides an accurate description of how particulates affect the optical properties of sea ice. Because we assumed absorption by the sediments to be similar to the values of *Carlson and Caverly* [1977], we chose for our calculations the $k_p(\lambda)$ that corresponds to $R_p = 9$ μm in Figure 8. In this case, there is strong absorption and a steep spectral gradient at shorter wavelengths and an absorption minimum at ~560 nm. However, it should be noted that other $[k_p(\lambda), R_p]$ pairs (e.g., those shown in Figure 8) could produce the same $\bar{\kappa}_p$ values and thus the same albedo predictions. Independent verification of our results would be possible if experimental data about $k_p(\lambda)$ and R_p could be obtained for the entrained sediments and atmospheric contaminants. In spite of the lack of such data, any of the derived $[k_p(\lambda), R_p]$ pairs can be used to calculate a reasonable $\bar{\kappa}_p$, regardless of which pair is most physically realistic.

The sensitivity studies show that the effects of particulates on the albedo of sea ice depend to a large degree on their vertical distribution within the sea-ice cover. Particulates entrained close to the surface produce a significant reduction in $\alpha(\lambda)$ at visible wavelengths, despite the usual presence of a relatively clean, highly scattering surface layer. However, layers of contaminated ice located deeper than 20–30 cm below the surface were found to have little effect on $\alpha(\lambda)$. In general, particulates derived either from sediments or from atmospheric deposition are redistributed vertically and laterally by meltwater during the summer months [*Pfirman et al.*, 1990; *Nürnberg et al.*, 1994; *Eicken et al.*, 1995] and tend to be concentrated just below the surface or at the bottom of melt ponds [*Pfirman et al.*, 1990; *Nürnberg et al.*, 1994] where they can have a major impact on $\alpha(\lambda)$.

Melting multiyear ice typically includes a decomposed surface layer (1–5 cm thick) underlain by a layer of bubbly and highly scattering ice that extends down to freeboard level. Normally, we would expect most of the particulates to be confined within these two layers. In melting first-year ice, there is again a thin (~1-cm thick) decomposed surface layer, but in this case it is underlain by much more vertically uniform and lower-scattering ice. While dust and soot would still be concentrated near the surface, the vertical extent of sediment loading in first-year ice can, depending on the amount of surface ablation experienced, be significantly greater than in multiyear ice. The effect of having lower-scattering ice would thus tend to enhance the ability of particulates deep within the ice to absorb light and further reduce $\alpha(\lambda)$. Because a snow cover effectively masks the presence of contaminated layers in the ice, effects of particulates on surface ablation and $\alpha(\lambda)$ are limited to the height of the ablation season when most or all of the snow has been removed. Even if not detectable in $\alpha(\lambda)$, the presence of particulates in the snow or underlying ice would still affect light transmission to the ocean and could thus impact biological activity in regions of first-year ice.

Our analysis has shown that although the ice controls scattering at all wavelengths even small amounts of particulates can alter the bulk absorption at visible wavelengths. This is because $\kappa_p(\lambda) \gg \kappa_i(\lambda)$ when $\lambda < 600$–700 nm (Figure 13a). Above 750 nm, absorption by the ice quickly becomes so large that the particulates no longer affect $\alpha(\lambda)$. Remote sensing techniques to estimate particulate loading in sea ice should therefore attempt to utilize information collected at visible wavelengths, preferably between 400 and 600 nm where differences between $\kappa_p(\lambda)$ and $\kappa_i(\lambda)$ are largest. Since both the magnitude and spectral shape of $\alpha(\lambda)$ are affected by the presence of particulates, the most feasible way to estimate the loading would be from reflectance data collected by aircraft or satellites. We expect the peak value of $\alpha(\lambda)$ to occur at the wavelength of minimum $\bar{\kappa}$, regardless of ice type. For clean ice this occurs at ~470 nm. In general, the wavelength of peak albedo will shift toward longer values as the total particulate loading increases. In the case of sediments, the wavelength of maximum albedo should approach 560 nm as loading becomes large. Also, as a result of a decrease in the magnitude of $\alpha(\lambda)$, spectral albedo gradients will become smaller in the red and near-infrared as particulate loading increases.

Although it should be possible to obtain at least a crude estimate of total loading from spectral albedo data and suitable assumptions about the distribution and properties of the particulates, more accurate estimates are complicated by a variety of factors. Ice structure, for example, can have a significant impact on how $\alpha(\lambda)$ is altered by the particulates. Especially important is proper characterization of the optical and physical properties (thickness, density, and average grain size) of the deteriorated layer. Also important is more detailed information on $k_p(\lambda)$ and on the in situ size distribution of the particulates. We found that optical properties in the visible are controlled by the fraction of the population that is clay and silt sized. The effect of sand-sized particles is negligible when compared to the effect of the smaller particles, so their mass will not show up directly in loading estimates derived from optical data. Our results suggest that standard sedimentological sample processing may tend to disaggregate larger particles that would optically be classified as sand sized when in situ. The actual mass represented by sand-sized particles is thus still uncertain at this point. It should also be stressed that sediment particles are optically thick, meaning that their effects on absorption must be determined from Mie theory and information about their size distribution, not by treating them as simple volume absorbers. Another issue that needs further study is how the presence of melt ponds would affect areally averaged loading estimates. Like particulates, ponds lower albedo; however, they do not alter the wavelength of maximum albedo.

This study has provided an indication of the quantitative importance of particulates, particularly ice-rafted sediments, on the albedo of arctic sea ice. Such information should be of value in developing remote sensing techniques to trace and

map the extent of sediment-laden ice. It is clear that entrainment of sediments and dust into sea ice, even in small amounts, can have a significant impact on the interaction of shortwave radiation with the summer ice pack. Further work on the optical properties of the particulates and on the structure of the upper 50 cm of the ice is needed to improve the prediction of the effects of particulate loading on the heat and mass balance of the ice cover.

Acknowledgments. This research was supported by the Office of Naval Research under Grants N00014-90-J-1075, N00014-94-1-0791, and N00014-97-1-0765. Support by a research grant from the German Ministry of Research and Technology (BMBF-Projekt "System Laptevsee") is also gratefully acknowledged. Ship personnel from the FS *Polarstern* and support by colleagues during the cruise were a great help in the collection of the field data. H. E. thanks Erk Reimnitz for freely sharing his profound knowledge about sea ice and sediments and providing support in various aspects of the field and laboratory work. M. Kuhn and F. Obleitner are thanked for supplying a spectral radiometer and numerous helpful suggestions. Finally, we would like to thank several anonymous reviewers whose insightful comments and suggestions contributed to substantial improvements in the presentation of this research.

References

Ackermann, N. L., H. T. Shen, and B. Sanders, Experimental studies of sediment enrichment of arctic ice covers due to wave action and frazil entrainment, *J. Geophys. Res.*, *99*, 7761–7770, 1994.

Barnes, P. W., E. Reimnitz, and D. Fox, Ice rafting of fine-grained sediment, a sorting and transport mechanism, Beaufort Sea, Alaska, *J. Sediment. Petrol.*, *52*, 493–502, 1982.

Barrie, L. A., R. M. Hoff, and S. M. Dagupatty, The influence of mid-latitudinal pollution sources on haze in the Canadian Arctic, *Atmos. Environ.*, *15*, 1407–1419, 1981.

Berger, E., Eichung eines Spektroradiometers, diploma thesis, Univ. of Innsbruck, Innsbruck, Austria, 1987.

Carlson, T. N., and S. G. Benjamin, Radiative heating rates for Saharan dust, *J. Atmos. Sci.*, *37*, 193–213, 1980.

Carlson, T. N., and R. S. Caverly, Radiative characteristics of Saharan dust at solar wavelengths, *J. Geophys. Res.*, *82*, 3141–3152, 1977.

Chylek, P., V. Ramaswamy, and V. Srivastava, Albedo of soot-contaminated snow, *J. Geophys. Res.*, *88*, 10,837–10,843, 1983.

Clark, D. L., and A. Hanson, Central Arctic Ocean sediment texture: A key to ice transport mechanisms, in *The Arctic Ocean Region*, edited by A. Grantz, L. Johnson, and J. F. Sweeney, pp. 301–330, Geol. Soc. of Am., Boulder, Colo., 1990.

Clark, R. N., and P. G. Lucey, Spectral properties of ice-particulate mixtures and implications for remote sensing, 1, Intimate mixtures, *J. Geophys. Res.*, *89*, 6341–6348, 1984.

Cox, G. F. N., and W. F. Weeks, Equations for determining the gas and brine volumes in sea ice samples, *J. Glaciol.*, *29*, 306–316, 1983.

Darby, D. A., L. H. Burckle, and D. L. Clark, Airborne dust on the Arctic pack ice, *Earth Planet. Sci. Lett.*, *24*, 166–172, 1974.

Driedger, C. L., Effect of ash thickness on snow ablation, in *The 1980 Eruptions of Mount St. Helens, Washington*, edited by P. W. Lipman, and D. R. Mullineaux, *U.S. Geol. Surv. Prof. Pap.*, *1250*, 757–760, 1981.

Eicken, H., M. Lensu, M. Leppäranta, W. B. Tucker III, A. J. Gow, and O. Salmela, Thickness, structure and properties of level summer multiyear ice in the Eurasian sector of the Arctic Ocean, *J. Geophys. Res.*, *100*, 22,697–22,710, 1995.

Eicken, H., R. Gradinger, B. Ivanov, A. Makshtas, and R. Pác, Surface melt puddles on multiyear sea ice in the Eurasian Arctic, in *World Climate Research Programme WCRP-94, Proceedings of the ACSYS Conference on the Dynamics of the Arctic Climate System (Göteborg, Sweden, 7–10 November 1994)*, *WMO/TD No. 760*, 267–271, World Meteorol. Org., Geneva, Switzerland, 1996.

Eicken, H., E. Reimnitz, V. Alexandrov, T. Martin, H. Kassens, and T. Viehoff, Sea-ice processes in the Laptev Sea and their importance for sediment export, *Cont. Shelf Res.*, *17*, 205–233, 1997.

Evans, B. T. N., Interactive program for estimating extinction and scattering properties of moist particulate clouds, *Rep. MRL-R-1123*, Def. Sci. and Technol. Organ., Mater. Res. Lab., Melbourne, Australia, 1988.

Gradinger, R., and D. Nürnberg, Snow algal communities on Arctic pack ice floes dominated by Chlamydomonas nivalis (BAUER) WILLE, in *Proceedings NIPR Symposium on Polar Biology*, vol. 9, pp. 35–43, Nat. Inst. of Polar Res., Tokyo, 1996.

Grams, G. W., I. H. Blifford Jr., D. A. Gillette, and P. B. Russell, Complex index of refraction of airborne soil particles, *J. Appl. Meteorol.*, *13*, 459–471, 1974.

Grenfell, T. C., The effects of ice thickness on the exchange of solar radiation over the polar oceans, *J. Glaciol.*, *22*, 305–320, 1979.

Grenfell, T. C., A theoretical model of the optical properties of sea ice in the visible and near infrared, *J. Geophys. Res.*, *88*, 9723–9735, 1983.

Grenfell, T. C., A radiative transfer model for sea ice with vertical structure variations, *J. Geophys. Res.*, *96*, 16,991–17,001, 1991.

Grenfell, T. C., and G. A. Maykut, The optical properties of ice and snow in the Arctic Basin, *J. Glaciol.*, *18*, 445–463, 1977.

Grenfell, T. C., and D. K. Perovich, Radiation absorption coefficients of polycrystalline ice from 400–1400 nm, *J Geophys. Res.*, *86*, 7447–7450, 1981.

Gribbon, P. W. F., Cryoconite holes on Sermikavsak, West Greenland, *J. Glaciol.*, *22*, 177–181, 1979.

Hansen, J. E., and L. D. Travis, Light scattering in planetary atmospheres, *Space Sci. Rev.*, *16*, 527–610, 1974.

Heintzenberg, J., Size-segregated measurements of particle elemental carbon and light absorption at remote Arctic locations, *Atmos. Environ.*, *16*, 2461–2469, 1982.

Henyey, L. G., and J. L. Greenstein, Diffuse radiation in the galaxy, *Astrophys. J.*, *93*, 70–83, 1941.

Higuchi, K., and A. Nagoshi, Effects of particulate matter in surface snow layers on the albedo of perennial snow patches, *IAHS Publ.*, *118*, 95–97, 1977.

Irvine, W. M., and J. B. Pollack, Infrared optical properties of water and ice spheres, *Icarus*, *8*, 324–360, 1968.

Ivanov, B., and V. Alexandrov, Albedo of the ice cover during late summer time and energy exchange processes, *Ber. Polarforsch.*, *149*, 47–51, 1994.

Kempema, E. W., E. Reimnitz, and P. W. Barnes, Sea ice sediment entrainment and rafting in the Arctic, *J. Sediment. Petrol.*, *59*, 308–317, 1989.

Larssen, B. B., A. Elverhøi, and P. Aagaard, Study of particulate material in sea ice in the Fram Strait—A contribution to paleoclimatic research?, *Polar Res.*, *5*, 313–315, 1987.

Ledley, T. S., and S. Pfirman, The impact of sediment-laden snow and sea ice in the Arctic on climate, *Clim. Change*, *37*, 641–664, 1997.

Ledley, T. S., and S. L. Thompson, Potential effect of nuclear war smokefall on sea ice, *Clim. Change*, *8*, 155–171, 1986.

Light, B., A structural-optical model of cold sea ice, M.S. thesis, Univ. of Wash., Seattle, 1995.

Lindberg, J. D., and L. S. Laude, Measurements of the absorption coefficient of atmospheric dust, *Appl. Opt.*, *13*, 1923–1927, 1974.

Maykut, G. A., and D. K. Perovich, MIZEX 84 heat and mass balance data, *Rep. 12-85*, Appl. Phys. Lab., Univ. of Wash., Seattle, 1985.

Mitchell, J. M., Visual range in the polar regions with particular reference to the Alaskan Arctic, *J. Atmos. Terr. Phys.*, *11*, suppl. 1, 195–211, 1957.

Nansen, F., Protozoa on the ice-floes of the North Polar Sea, in *The Norwegian North Polar Expedition 1893–1896: Scientific Results*, vol. 5, part 16, edited by F. Nansen, 22 pp., Longmans, Green, Toronto, Ont., 1906.

Noone, K. J., and A. D. Clarke, Soot scavenging measurements in arctic snowfall, *Atmos. Environ.*, *22*, 2773–2778, 1988.

Nürnberg, D., I. Wollenburg, D. Dethleff, H. Eicken, H. Kassens, T. Letzig, E. Reimnitz, and J. Thiede, Sediments in Arctic sea ice—Implications for entrainment, transport and release, *Mar. Geol.*, *119*, 185–214, 1994.

Osterkamp, T. E., and J. P. Gosink, Observations and analyses of sediment-laden sea ice, in *The Alaskan Beaufort Sea: Ecosystems and Environments*, edited by P. W. Barnes, D. M. Schell, and E. Reimnitz, pp. 73–93, Academic, San Diego, Calif., 1984.

Patterson, E. M., D. A. Gillette, and B. H. Stockton, Complex index of refraction between 300 and 700 nm for Saharan aerosols, *J. Geophys. Res.*, *82*, 3153–3160, 1977.

Perovich, D. K., and A. J. Gow, A quantitative description of sea ice inclusions, *J. Geophys. Res.*, *101*, 18,327–18,343, 1996.

Pfirman, S., I. Wollenburg, J. Thiede, and M. A. Lange, Lithogenic sediment on Arctic pack ice: Potential aeolian flux and contribution to deep sea sediments, in *Paleoclimatology and Paleometerology: Modern and Past Patterns of Global Atmospheric Transport*, edited by M. Leinen, and M. Sarnthein, pp. 463–493, Kluwer Acad., Norwell, Mass., 1989.

Pfirman, S., M. A. Lange, I. Wollenburg, and P. Schlosser, Sea ice characteristics and the role of sediment inclusions in deep-sea deposition: Arctic–Antarctic comparisons, in *Geological History of the Polar Oceans: Arctic Versus Antarctic*, edited by U. Bleil, and J. Thiede, pp. 187–211, Kluwer Acad., Norwell, Mass., 1990.

Podgorny, I. A., and T. C. Grenfell, Absorption of solar energy in a cryoconite hole, *Geophys. Res. Lett.*, *23*, 2465–2468, 1996.

Pope, R. M., and E. S. Fry, Absorption spectrum (380–700 nm) of pure water, II, Integrating cavity measurements, *Appl. Opt.*, *36*, 8710–8723, 1997.

Reimnitz, E., Sediments in sea ice, *Ber. Polarforsch.*, *149*, 69–73, 1994.

Reimnitz, E., E. W. Kempema, W. S. Weber, J. R. Clayton, and J. R. Payne, Suspended-matter scavenging by rising frazil ice, in *Sea Ice Properties and Process*, *CRREL Monograph 90-1*, edited by S. F. Ackley and W. F. Weeks, pp. 97–100, Cold Reg. Res. and Eng. Lab., Hanover, N. H., 1990.

Reimnitz, E., M. McCormick, K. McDougall, and E. Brouwers, Sediment export by ice rafting from a coastal polynya, Arctic Alaska, U.S.A., *Arct. Alp. Res.*, *25*, 83–98, 1993.

Roesler, C. S., and R. Iturriaga, Absorption properties of marine-derived material in Arctic sea ice, in *Ocean Optics XII*, edited by J. S. Jaffe, Proc. SPIE Int. Soc. Opt. Eng., *2258*, 933–943, 1994.

Roesler, C. S., M. J. Perry, and K. L. Carder, Modeling in situ phytoplankton absorption from total absorption spectra in productive inland marine waters, *Limonl. Oceanogr.*, *34*, 1510–1523, 1989.

Rosen, H., T. Novakov, and B. A. Bodhaine, Soot in the Arctic, *Atmos. Environ.*, *15*, 1371–1374, 1981.

Smith, R. C., Optical properties of the Arctic upper water, *Arctic*, *26*, 303–313, 1973.

Smith, R. C., and K. S. Baker, Absorption coefficients of the clearest natural waters, *Appl. Opt.*, *20*, 177–184, 1981.

SooHoo, J. B., A. C. Palmisano, S. T. Kottmeier, M. P. Lizotte, S. L. Soo Hoo, and C. W. Sullivan, Spectral light absorption and quantum yield of photosynthesis in sea ice microalgae and a bloom of *Phaeocystis Pouchetii* from McMurdo Sound, Antarctica, *Mar. Ecol. Prog. Ser.*, *39*, 175–189, 1987.

Warren, S. G., Optical properties of snow, *Rev. Geophys.*, *20*, 67–89, 1982.

Warren, S. G., Impurities in snow: Effects on albedo and snowmelt, *Ann. Glaciol.*, *5*, 177–179, 1984.

Warren, S. G., and W. J. Wiscombe, Dirty snow after nuclear war, *Nature*, *313*, 467–470, 1985.

Weeks, W. F., and S. F. Ackley, The growth, structure, and properties of sea ice, in *The Geophysics of Sea Ice*, edited by N. Untersteiner, pp. 9–164, Plenum, New York, 1986.

Wollenburg, I., Sedimenttransport durch das arktische Meereis: Die rezente lithogene und biogene Materialfracht, *Ber. Polarforsch.*, *127*, 1–159, 1993.

Woo, M.-K., and M.-A. Dubreuil, Empirical relationship between dust content and arctic snow albedo, *Cold Reg. Sci. Technol.*, *10*, 125–132, 1985.

Zaneveld, J. R. V., D. M. Roach, and H. Pak, The determination of the index of refraction distribution of oceanic particulates, *J. Geophys. Res.*, *79*, 4091–4095, 1974.

H. Eicken, Geophysical Institute, University of Alaska Fairbanks, Fairbanks, AK 99775.

T. C. Grenfell, B. Light, and G. A. Maykut, Department of Atmospheric Sciences, University of Washington, Seattle, WA 98195. (e-mail: maykut@atmos.washington.edu)

(Received December 30, 1997; revised July 16, 1998; accepted July 24, 1998.)